

Full Length Research Paper

Characterization of the top sediment layer in coastal intertidal mudflats from medium-to-coarse resolution satellite imagery and field measurements

Timothy Dube^{1,2*}, Tawanda W. Gara¹, Webster Gumindoga², Emmerson Chivhenge¹ and Tsikai S. Chinembiri³

¹Department of Geography and Environmental Science, University of Zimbabwe, P.O Box MP 167, Mt Pleasant, Harare.

²University of KwaZulu-Natal, School of Agriculture, Engineering and Science, Private Bag X01, Scottsville, 3209 South Africa.

³Department of Civil Engineering, University of Zimbabwe, P.O. Box MP 167, Mt Pleasant, Harare, Zimbabwe.

⁴Ministry of Lands and Rural Resettlement, P.Bag 7779 Causeway, Harare, Zimbabwe.

Accepted 21 November, 2013

Intertidal sediments are critically important in controlling intertidal mudflat microphytobenthic primary productivity and the functioning of intertidal ecosystems. This paper demonstrates the possibility of deriving different intertidal sediment properties from coarse-to-medium resolution remote sensing imagery. Supervised and image based classification methods were used to map different substrate types based on the Spectral Angle Mapper (SAM) algorithm. The algorithm characterized different sediment properties from remote sensing data based on field collected and image-extracted endmembers. The results demonstrate that, different substrate types can be derived from coarse-to-medium resolution images using SAM algorithm. Supervised and image-based classification methods performed well in deriving intertidal sediment properties. From the results, sand sediments cover a wide area in extent than clay whereas Normalized Difference Vegetation Index (NDVI) validation results indicate that, clay sediments have higher NDVI values as compared to sand sediments. We conclude that, intertidal sediment properties can be successfully derived from coarse-to-medium resolution satellite imagery.

Key words: Endmember, microphytobenthos, spectral signature, substrates, trios ramses, wadden sea.

INTRODUCTION

Deriving information on intertidal mudflats sediment properties is critical for understanding and making inferences on the functionality of intertidal ecosystems, as well as understanding levels of sediment stability and sedimentation (Jesus et al., 2006). Familiarity with intertidal sediment characteristics helps in understanding the spatial and temporal variability in microphytobenthic chlorophyll-a (chl-a) content and microphytobenthic primary productivity. Ecologically, intertidal mudflat sediment surfaces are a habitat to pelagic and benthic

micro-organisms or micro-algae capable of forming biofilms and microbial mats, and which are responsible for intertidal primary productivity as well as sediment stability through the secretion of extracellular polymeric substances (EPS) (Paterson et al., 2001; Stal, 2010). EPS glue sediment grains together, resulting in stabilization of estuarine sediments from tidal suspension (Adam et al., 2009; Blanchard, 2000; Kromkamp et al., 2006). In this regard, the existence of intertidal mudflats is bio-physically and ecologically crucial to coastal ecosystems.

Despite the bio-physical and ecological significance of intertidal mudflats, the existence of intertidal mudflats is currently threatened by phenomena such as climate change which cause sea level rise. In addition, physical human development emanating from regular shipping activities also causes alterations in sedimentation patterns (CPSL, 2005; Reise et al., 2010). Intertidal mudflats are normally characterized as coastal wetlands that result from prolonged and consistent deposition of nutrient-rich estuarine silts, clays, or sand particles, and marine animal detritus by tides and rivers in shallow areas or within the intertidal zone (Adam et al., 2009; Reise et al., 2010). In intertidal mudflats, sediment sizes vary from nutrient-poor coarse sand with grain size stretching from 63 μm to 2 mm (Adam et al., 2009), to nutrient-rich silt and fine clay or mud with particles less than 62.5 μm (Stal, 2010).

Although, intertidal sediments surfaces have an undisputable ecological role, our knowledge on the spatial distribution of intertidal sediment properties is limited. This limitation is related to problems linked to field measurements such as area inaccessibility (Jesus et al., 2006), the patchy nature of their occurrence (Adam et al., 2009; Jesus et al., 2006; Kromkamp et al., 2006; Smith et al., 2004) and the cost of fine resolution satellite remote sensing data. According to Adam et al. (2011), field measurements on intertidal mudflat sediment surfaces are tedious, expensive, labour-intensive, ecologically destructive and also do not fully capture the spatial heterogeneity since they are conducted at point basis. Moreover, field measurements on intertidal mudflat areas are also affected by the unpredictable tidal cycle. In the light of the above, the advent of satellite remote sensing techniques offers a better alternative means of obtaining essential information to study intertidal mudflats (Adam et al., 2009; Deronde et al., 2006; Murphy et al., 2008; van der Wal et al., 2004). Satellite remote sensing data has the capability of providing a consistent and full spatio-temporal coverage of intertidal mudflat areas. The technique also provides non-intrusive measurements of areas considered to be inaccessible and highly sensitive to any physical disturbances such as trampling. Remote sensing and GIS techniques enhance spatio-temporal investigations on the ecological and physical characteristics of the environment by providing a synoptic view of intertidal areas at minimal costs (van der Wal et al., 2010). To the best of our knowledge, intertidal sediment properties have been derived from fine resolution satellite remote sensing data such as HyperMapTM (Hyper spectral Mapper) scanner and the Airborne Hyperspectral Sensor (AHS) on board of the CASA 212-200 aerial platform with a spatial resolutions ranging from 3 to 10 m (Adam et al., 2009). This study explores the possibility of using coarse-to-medium resolution images such as the Advanced Spaceborne Thermal Emission and Reflection Radiometer (ASTER), Landsat Thematic Mapper (TM5) and Medium Resolution

Imaging Spectrometer (MERIS) in order to derive different intertidal substrate types in the Wadden Sea. Accurate mapping of different intertidal substrate types in the Wadden Sea is critical for sustainable monitoring and management of these fragile ecosystems.

MATERIALS AND METHODS

Study area

This study was conducted in the Dutch Wadden Sea (the Netherlands). The sea is a shallow open estuarine intertidal region (CPSL, 2005). It has an areal coverage of approximately 10,000 km^2 and about 500 km in length (Hogan, 2011; Hommersoms, 2010). In June 2009, the Wadden Sea was included in the World Heritage list by UNESCO (Hommersoms, 2010; UNEP, 2009) because of its unique ecological, economic and societal significance (Otto et al., 2001). Its ecological significance is mostly centered on biological diversity that is based on coastal habitats such as intertidal mudflats (Reise et al., 2010).

The Wadden Sea experiences temperate climatic conditions defined by the convergence of two different air masses that result in mild winters and cooler summers (UNEP, 2009). Although the sea is the source of humid air, precipitation in the Wadden Sea area is moderate, ranging from 700 to 800 mm yr^{-1} or approximately 2 mm d^{-1} (UNEP, 2009). The Wadden Sea landscape is made up of flat coastal plains and the lowly-elevated offshore barrier islands with an altitude of approximately ± 50 m above sea level. Coastal sand dunes, beach ridges and dykes constitute the main topographic types in the area (UNEP, 2009) (Figure 1)

Field radiometric measurements

In-situ field radiometric measurements were conducted between the 26th and 28th of September 2011. Measurements were done on exposed intertidal mudflat sediment surfaces following the predicted tidal cycle (Figure 2) using the Trios RAMSES sensors. The sensors measured upwelling radiance ($\text{Wm}^{-2} \text{sr}^{-1} \text{nm}^{-1}$) and the downwelling irradiance ($\text{Wm}^{-2} \text{nm}^{-1}$). Intertidal mudflats properties were divided into three (3) types that is, sand, clay, and sea weeds. Coordinates of the intertidal mudflat sites sampled at low tide are shown in Table 1. Field measurements were specifically done on undisturbed sediment surfaces so as to capture an undistorted reflectance from intertidal sediment surfaces. Downwelling irradiance $E_d(O^*, \lambda)$ was measured at an angle of 135° and upwelling radiance $L_u(O^*, \lambda)$ with an angle of 40° and a field of view of 7°. All these measurements were done simultaneously from a fixed height of 110 cm above the intertidal surface sediments so as to increase the radiometric footprint. Spectral signature values were assessed for consistence through plotting spectral graphs against wavelength in the field (Figure 3). The coordinates of the sampling sites were recorded using a handheld Global Position System (GPS) receiver (with an error of ± 3 m) and imported to a GIS environment. For radiometric measurements, a stratified random approach was used to select 37 locations on 3 different sites to capture the inherent sediment spatial heterogeneity.

Remote sensing data acquisition

Selected remote sensing imagery that is, ASTER, Landsat TM5, and MERIS, with a spatial resolution of 15, 30, and 300 m, respectively were used. Landsat images were acquired from the

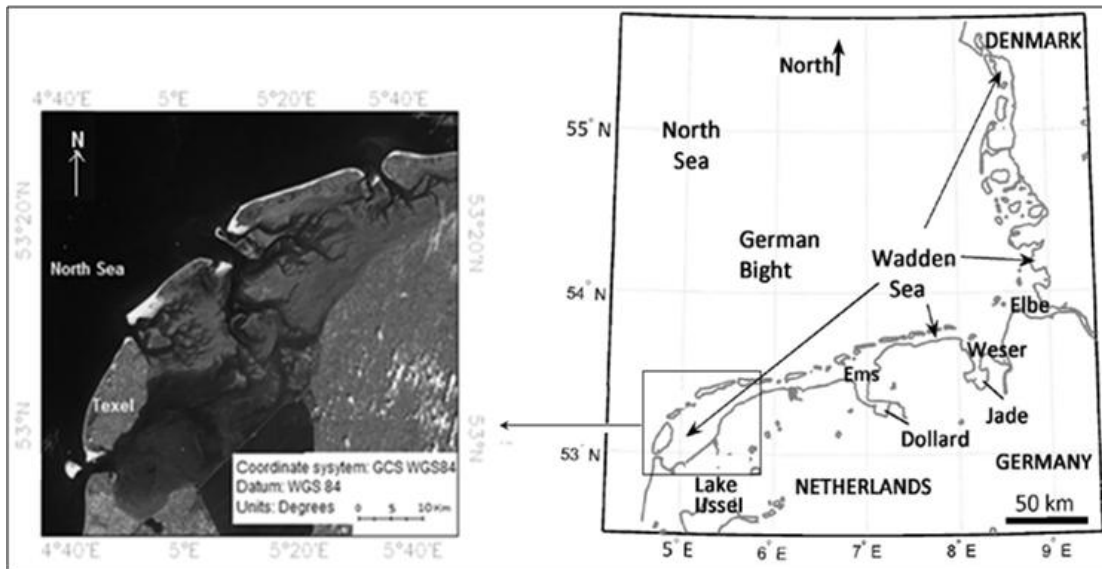


Figure 1. False- colour composite map of the Wadden Sea with special reference to the Dutch part (Source: ASTER 2007).

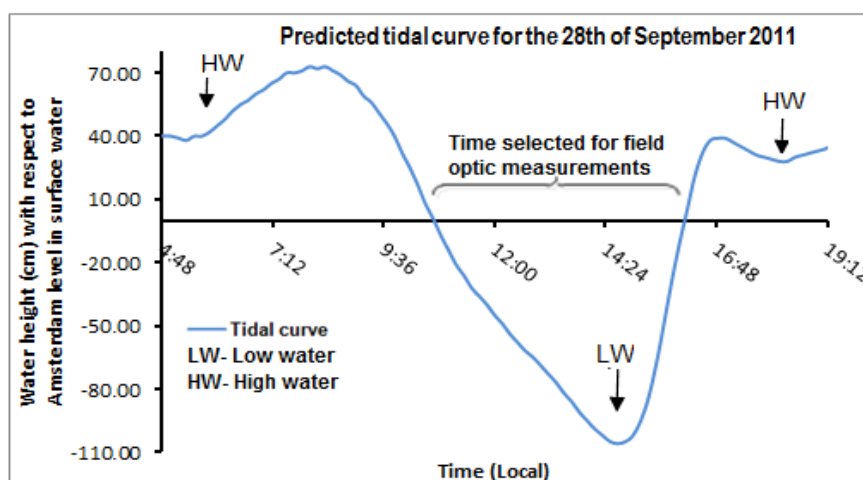


Figure 2. Predicted tidal cycle followed in undertaking field radiometric measurements.

Table 1. Coordinates of the intertidal mudflat sites sampled at low- tide

Date	Station	Lat. N	Long. E	Location	Sample points
26.09.2011	Site 1	53°2.460	04°58.426	Lutjeswaard	6
27.09.2011	Site 2	53°4.193	04°53.181	Vlakte van Kerken	13
28.09.2011	Site 3	52°57.225	04°50.213	Balgzand	18

readily available online Landsat archive, that is, via the United States Geological Survey Global Visualization Viewer (GloVis) (<http://glovis.usgs.gov/> web-link). ASTER level 1B images were acquired via the ITC RSG lab, whereas MERIS images were acquired from European Space Agency (ESA). Cloud-free images

were acquired during a period of low tide. To confirm whether the images were collected during a period of low tide we retrieved information on tidal water height from an online tidal database. Den Helder which is in the Western part of Wadden Sea was used as the reference for the whole area under study.

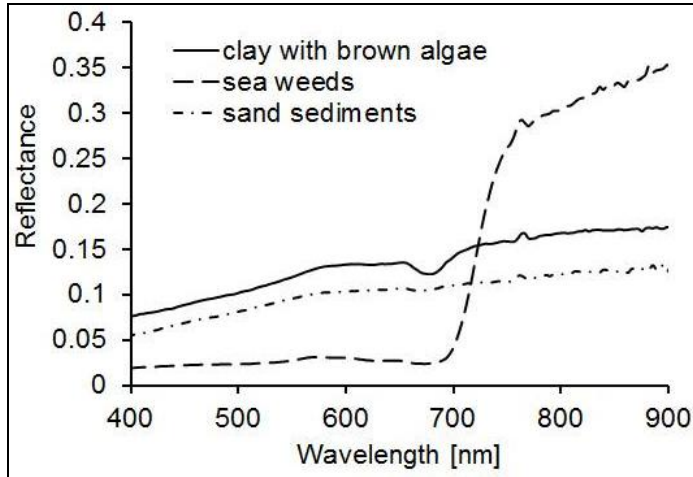


Figure 3. Three spectral signatures derived from intertidal sediment properties.

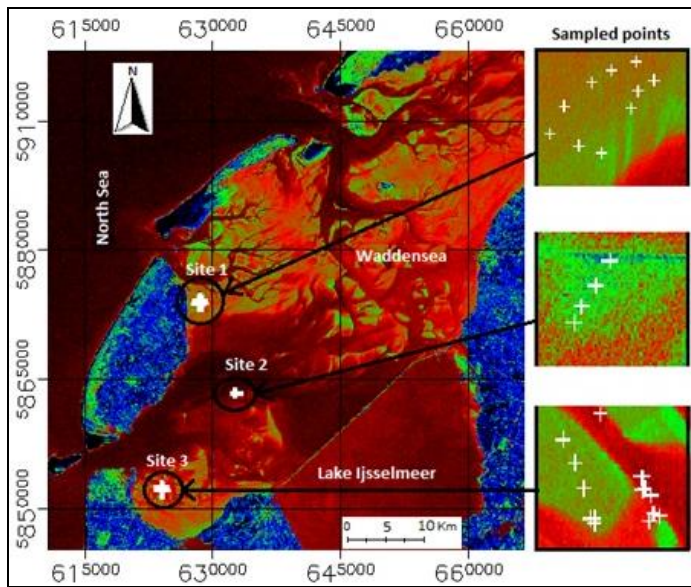


Figure 4. Map showing adopted field sampled site.

Field data preprocessing

Downwelling irradiance and upwelling radiance derived from the Trios RAMSES sensors were used to derive the remote sensing reflectance for sand, clay and sea weeds (Figures 5 to 7). Remote sensing reflectance was determined directly by computing the ratio of upwelling radiance and downwelling irradiance as shown in Equation 1.

$$Rrs = \frac{L_u(0^+, \lambda)}{E_d(0^+, \lambda)}, \quad [sr^{-1}] \quad (1)$$

Where: Rrs = remote sensing reflectance [sr^{-1}], $L_u(0^+, \lambda)$ = upwelling radiance [$Wm^{-2} sr^{-1} nm^{-1}$], $E_d(0^+, \lambda)$ = downwelling irradiance [$Wm^{-2} nm^{-1}$].

Remote sensing reflectance was converted to spectral reflectance by multiplying the resultant output by pi (π) in order to derive information on sediment types. Three spectral end member types were determined and these were used for ecotopy mapping. This spectral end member refers to a specific pure spectral feature acquired through *in situ* radiometric measurements or laboratory analysis of reflectance spectra; principally focusing on a single surface (Hommersoms, 2010; Schwengerdt, 1997; Yuhans et al., 1992).

Remote sensing data calibration

Landsat images were acquired in Digital Number (DN) format. However, for these images to be used in deriving information on mudflat substrate types, firstly they had to be calibrated into spectral radiance units [$Wm^{-2}sr^{-1}\mu m^{-1}$] following the calibration method by Chander et al. (2009). The calibration coefficients were provided together with the respective Landsat images. The conversion from DN to spectral radiance was done band by band. ASTER level 1B contains radiometrically-calibrated and geometrically co-registered data (YCEO, 2011). MERIS level 1B were readily geometrically calibrated so as to be matched with the Top-Of-Atmosphere (TOA) radiance.

Atmospheric correction of remote sensing data

The visible bands for Landsat TM5 and ASTER images were atmospherically-corrected using the Fast Line-of-sight Atmospheric Analysis of Spectral Hypercubes (FLAASH) model (Felde et al., 2003; Kaufmann et al., 1997) which is only applicable to 0.35 to 2.5 μm visible region of the electromagnetic wavelength. The FLAASH model, an interface of the ENVI GIS software, is recommended for retrieving reflectance from multispectral radiance images (Kaufmann, et al., 1997; Trishchenko, et al., 2002). On the other hand, MERIS images were corrected for atmospheric effects using Simple Method for Atmospheric Correction (SMAC) in the BEAM software (ESA, 2012). SMAC is a semi-empirical approximation of the radiative transfer in the atmosphere (Rahman et al., 1994). FLAASH and SMAC incorporates the MODTRAN4 radiation transfer code (Berk, 2000) which involves the application of a correlated-k algorithm which significantly enables precise computation of various scattering.

Image classification algorithm

The supervised and image-based classification methods were implemented using spectral angle mapper (SAM) algorithm (Boardman 1994; Brotas, et al., 1995). The SAM algorithm is expressed in Equation 2:

$$\alpha = \cos^{-1} \left(\frac{\sum_{i=1}^{nb} t_i r_i}{\sqrt{\sum_{i=1}^{nb} t_i^2 \sum_{i=1}^{nb} r_i^2}} \right), \quad (2)$$

where: nb = number of bands, t_i = unknown spectra and r_i = known spectra.

The algorithm classifies images by comparing the unknown image spectra with the known spectra (De Carvalho et al., 2000; Kruse et al., 1992) as shown in Figure 4. The resultant outputs of SAM, were classified images with the best match at each pixel, measured in radians ranging from 0 to $\pi/2$ (Kruse et al., 1993). Derivation of endmembers from remote sensing data was done using the Pure

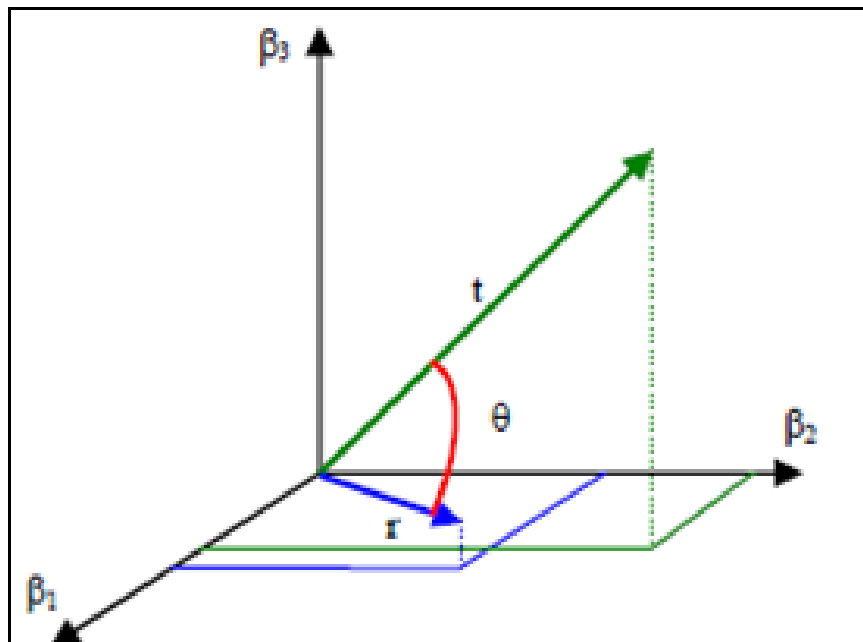


Figure 5. SAM algorithm Concept

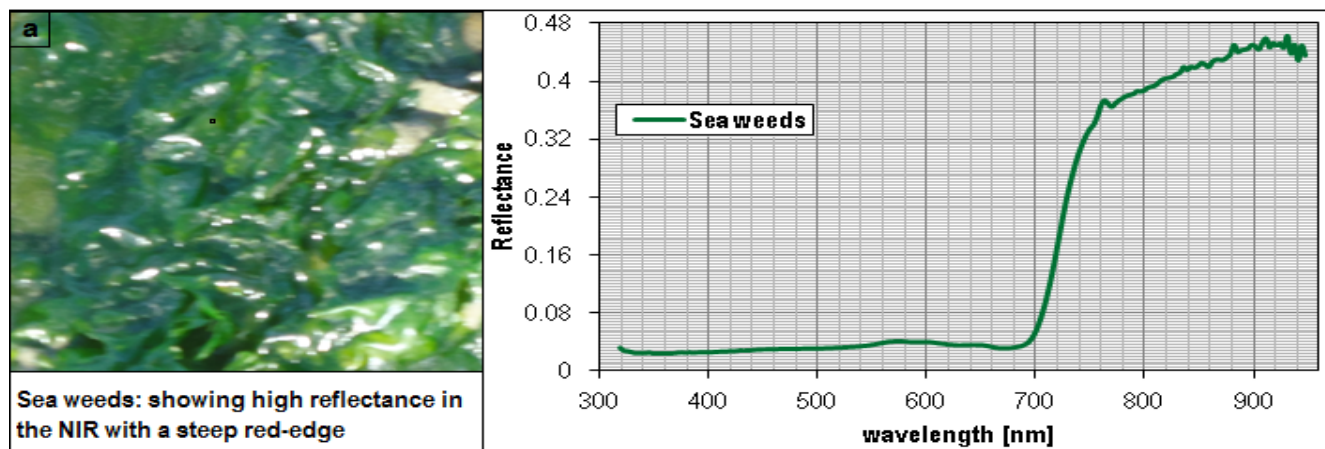


Figure 6. Spectral signature for sea weeds in intertidal mudflats of Wadden sea.

Pixel Index (PPI). Before this algorithm was implemented, the inherent remote sensing data was reduced using the Minimum Noise Fraction (MNF) transformation method (Boardman 1994). The MNF transformation method defines the inherent data dimensionality through separating and equally distributing the noise within data (Boardman and Kruse, 1994). The method ensured that, the data variance declined with an increase in the number of bands. The decrease in data variance continued until only noise and none coherent image bands remained. For the PPI method that was used for multi-spectral endmember extraction, a value of 19.5 for the number of PPI, and a PPI threshold value of 8.5 was used. The smaller number of PPI was selected because it showed only purest pixels as compared to a large number. The PPI computation identified and grouped purest pixels in the n-dimensional space. The purest pixels are associated with bright pixels in the image

(Chaudhry, et al., 2006).

Normalised difference vegetation index (NDVI)

NDVI is a numerical indicator often used as a proxy for estimating chl-a concentration in mudflats from remotely-sensed data (Kromkamp et al., 2006). In analyzing remote sensing data; the index uses the visible (VIS), red (0.4 to 0.7 μm), and near-infrared (NIR) bands (0.75 - 1.1 μm) of the electromagnetic spectrum (Rulinda et al., 2010; Tucker, 1979). The index determines chl-a concentration based on Equation 3. When the difference between the NIR and the red reflectance is large it means that, the concentration of chl-a is very high and the reverse is true. NDVI values range from -1 through 0 to 1.

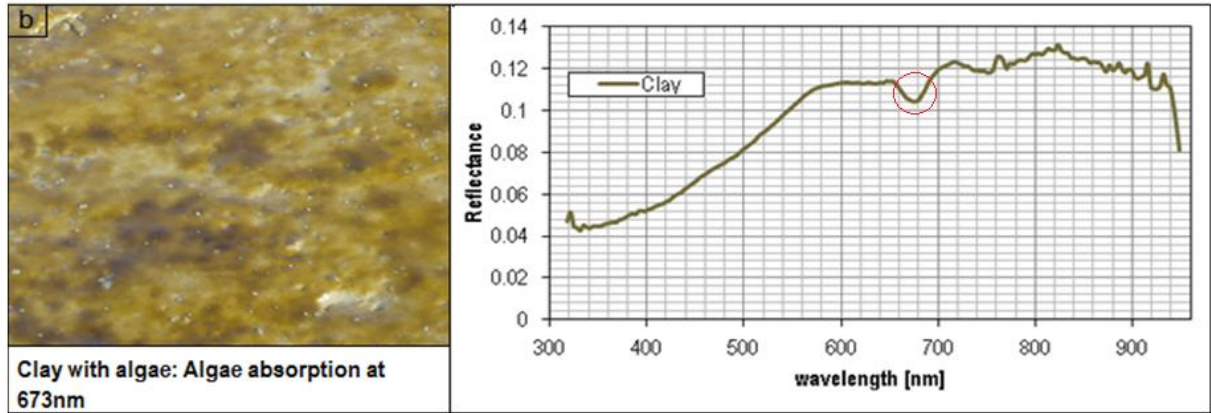


Figure 7. Spectral signature for clay sediments in intertidal mudflats of Wadden sea.

$$NDVI = \frac{\rho_{NIR} - \rho_{RED}}{\rho_{NIR} + \rho_{RED}} \quad (3)$$

Where: ρ_{NIR} = chl-*a* maximum reflectance in the near-infrared wavelength; and ρ_{RED} = maximum absorption in the red band.

Thus, based on the above equation, NDVI was calculated as follows:

$$\begin{aligned} \text{Landsat TM5} &= (B_{840} - B_{660}) / (B_{840} + B_{660}); \\ \text{ASTER} &= (B_{807} - B_{661}) / (B_{807} + B_{661}); \\ \text{MERIS} &= (B_{865} - B_{665}) / (B_{705} + B_{665}). \end{aligned}$$

RESULTS AND DISCUSSION

Field spectral reflectance curves

Figures 5, 6, and 7 present the different spectral signatures for sea weeds, clay and sand substrates across the Wadden Sea. It can be observed that, sea weeds spectral signature is characterized by low reflectance values in the visible spectrum (VIS) with approximately 0.0025 between 400 to 700 nm and around 0.3 to 0.35 in the near infra-red (NIR) bands. A steep red edge between the visible and near infra-red bands was observed. Low reflectance values in the visible spectral region are a result of high absorption of radiation by chlorophyll-*a*, whereas high reflectance values in the near-infra-red are due to the seaweed blade internal scattering and no absorption. Spectral trends in the VIS and NIR imply that seaweeds have some concentrations of photosynthetic pigments that absorb light in the visible range at the same time reflecting much in the longer wavelength.

Spectral signature for clay sediments with algae display a steep rise between 400 to 550 nm and a strong chl-*a* absorption dip at 673 nm. However at 700 nm, the reflectance spectra turns to be smooth, without much

change. This implies that the spectral signature was not affected by the presence microphytobenthos (MPB) within clay sediments. This spectral dip at 673 nm is expected and most probably explained by the presence of microphytobenthic diatoms in clay sediments which significantly said to contribute to mudflat biomass. Adam et al. (2009) conducted similar field measurements using ASD spectrometer and attained similar spectral trends over clay sediments, with high absorption around 673 nm. Actually, literature shows that when there is no microphytobenthic biomass content within sediments, the spectral profile will be somehow smooth indicating no absorption troughs (Adam et al., 2009). In a different study by Kromkamp et al. (2006) found that, sediments dominated by MPB diatoms had a sharp spectral reflectance at around 500 nm with an absorption dip at 675 nm resulting from chl-*a* absorption within that spectral region (Figure 6).

Spectral reflectance for sandy sediments demonstrates a different spectral signature, with low values with almost smooth spectral reflectance signature (maximum reflectance around 0.18) when compared to that for clay (~ 0.35). It is assumed that, this observation maybe as a result of low microphytobenthic content in sand substrate. Sands tend to be both lower in nutrients and more frequently resuspended than cohesive clay sediments, and these characteristics probably contribute towards lower MPB biomass. This remark is also confirmed by a smooth trend in the spectral reflectance profile with less chl-*a* absorption dip at 673 nm throughout the spectral range as observed in Figure 8. However, minor absorption residuals that can be recognized around 673 nm are a result of the presence of MPB diatoms within sandy substrates. In general, a clear-cut distinction amongst different endmembers from different substrate types is observed. These differences can be attributed to the variability in algal /or MPB content available in different substrate types. According to Carrère et al. (2004), the amount of absorption in different sediment spectra is directly a function of chl-*a* concentration

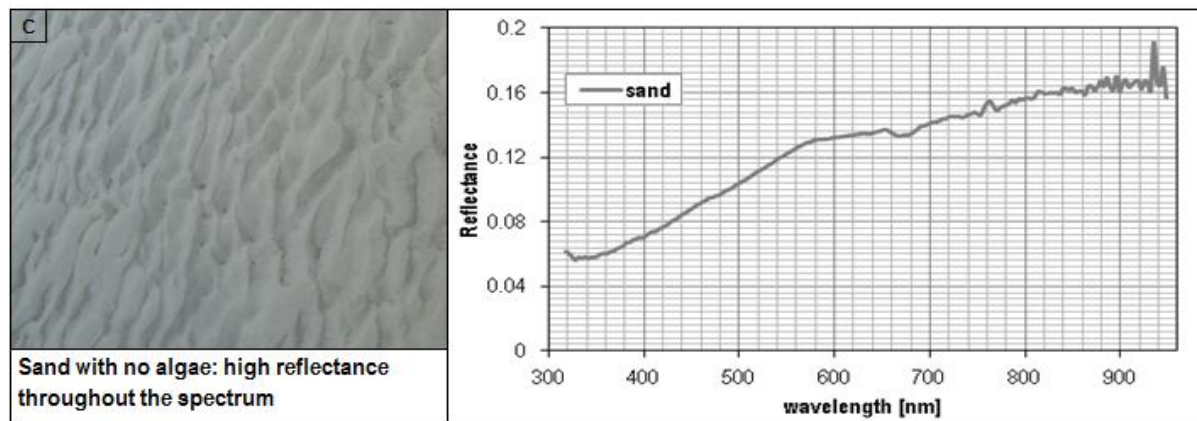


Figure 8. Spectral signature for sand sediments in intertidal mudflats of Wadden sea

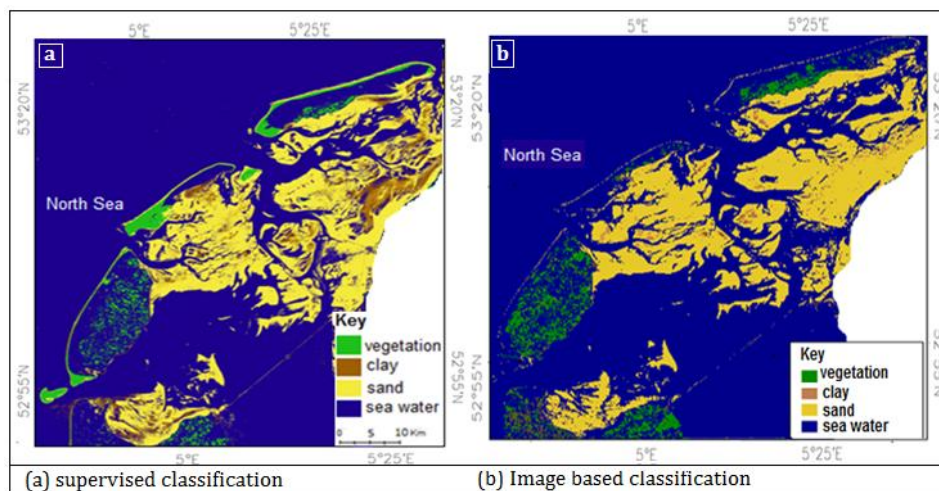


Figure 9. Intertidal mudflats sediment classes derived from Landsat 2000 using SAM.

detected in different substrates. Although, natural and expected spectral patterns can be observed, the purity of these spectral signatures seems to be largely compromised by substrate moisture effects and its significant radiation absorption (Figure 7)

Intertidal substrate types

The results in Figure 14 indicate clay and sand sediments classes derived from Landsat TM, ASTER and MERIS images respectively. The sediments were characterized from remotely sensed data using field-derived spectral signatures (Figures 5 to 7). From these results it can be further observed that, both clay and sand sediments significantly vary spatially across the entire intertidal area. Although, there is spatial variability of both sediments, a close examination of results shows that, clay sediments present a lesser spatial extension than sand. This is because substrates within the intertidal area are

constantly exposed to suspension and further destabilization by waves and tidal currents, resulting in washing away of interstitial/pore-water nutrients leaving behind vast areas covered by sand. It can also be realized that, in the year 2000 there was a more pronounced clay and sand content over the entire Wadden Sea area (Figure 8). It can also be observed that, across the entire region sandier and clay sediments were detected in the north eastern and south western regions. Limited detections were made in the central region of the Wadden Sea probably due to high water levels submerging the mudflats during the satellite overpass period.

From both supervised classification and image-based classification results; it can be observed that, more clay sediments have been derived from the image based classification method than the later (Figures 9, 10, 11, 12, and 13). A similar clay and sand sediment distribution trend is observed on both classification results from MERIS 2011. In Figure 14, both image-based classification

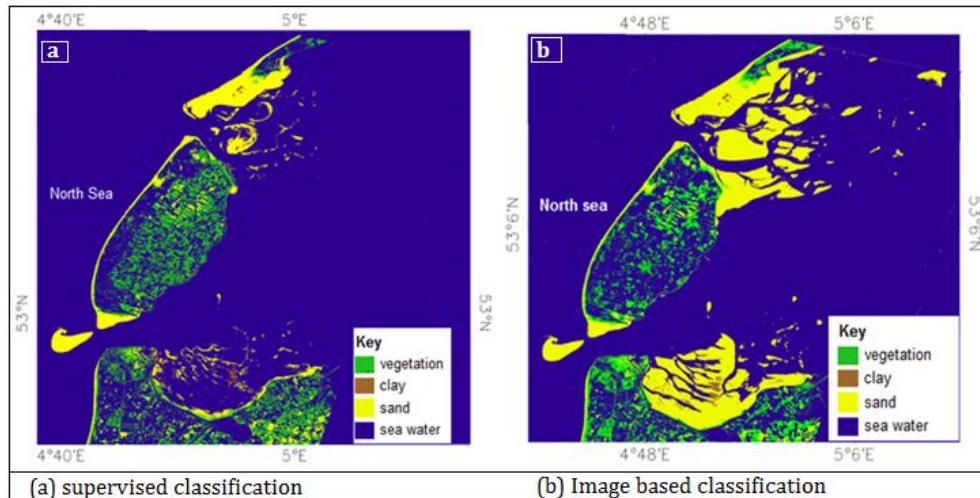


Figure 10. Intertidal mudflats sediment classes derived from Landsat 2003 using SAM.

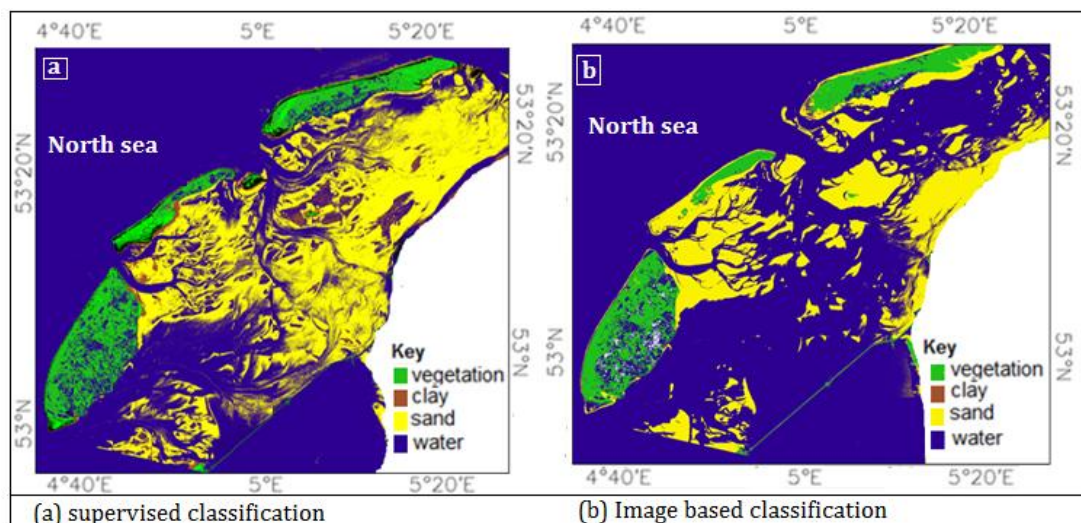


Figure 11. Intertidal mudflats sediment classes derived from Aster 2007 using SAM.

and supervised classification demonstrates a similar distribution of sand and clay sediments although not giving a one-on-one match-up. This observation can be attributed to the fact that, field-collected endmembers may be affected by the prevailing environmental factors. For instance, the presence of thin water films can largely compromise the purity field collected spectral endmembers. However, this limitation can be improved either through undertaking laboratory analysis of substrate reflectance spectral signatures (Schwengerdt, 1997) or by using analytical methods like x-ray or microprobe analysis (Clark et al., 1993; Kempeneer et al., 2006) because these procedures would minimize the influence of environmental factors on reflectance. However, the fact that image-based classification may

have overestimated the substrates content within intertidal mudflats may not be ruled out.

Validation of substrates properties with spatial variation of NDVI

Table 2 illustrates a summary of statistics computed from all the image-based classification results to accuracy for assessment. It can be noted that, NDVI values are high on seaweed substrates, followed by those on clay substrates, which is to be expected, since clay substrates have higher concentrations of organic matter and microphytobenthic organisms (Dube, 2012). The highest NDVI value (0.71) was recorded in year 2000 from Landsat

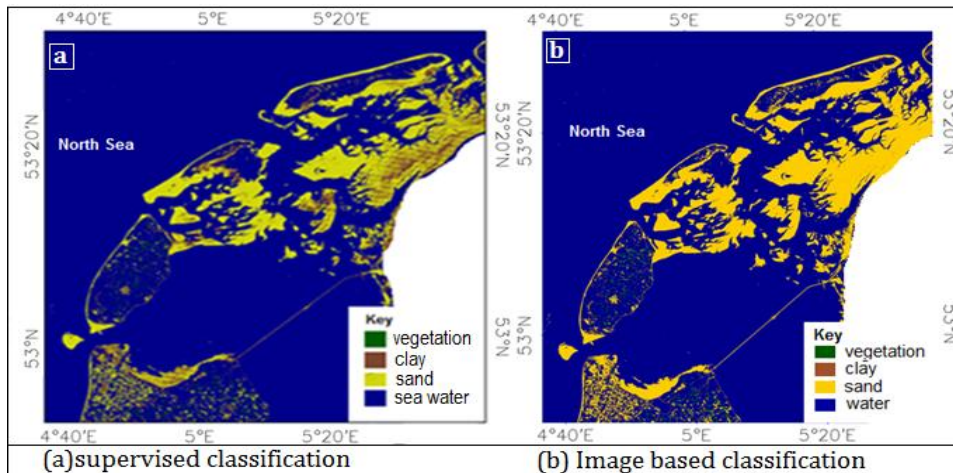


Figure 12. Intertidal mudflats sediment classes derived from Landsat TM 2009 using SAM.

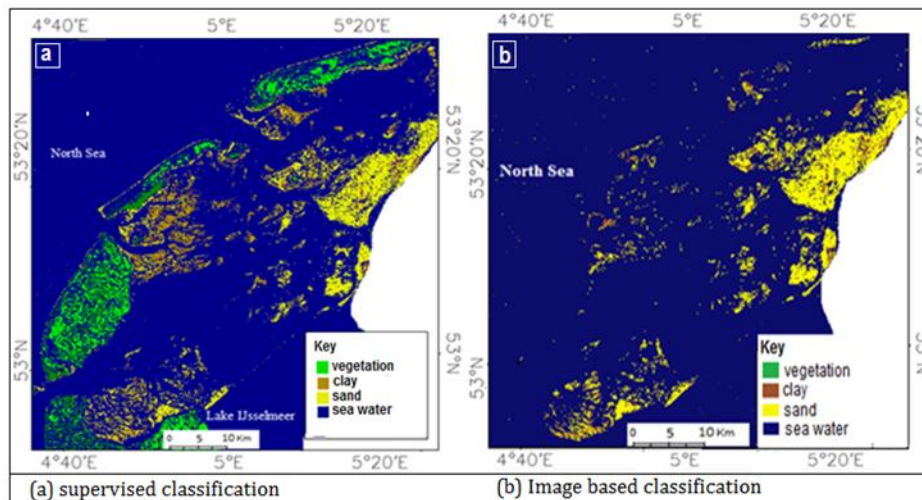


Figure 13. Intertidal mudflats sediment classes derived from Landsat TM 2010 using SAM.

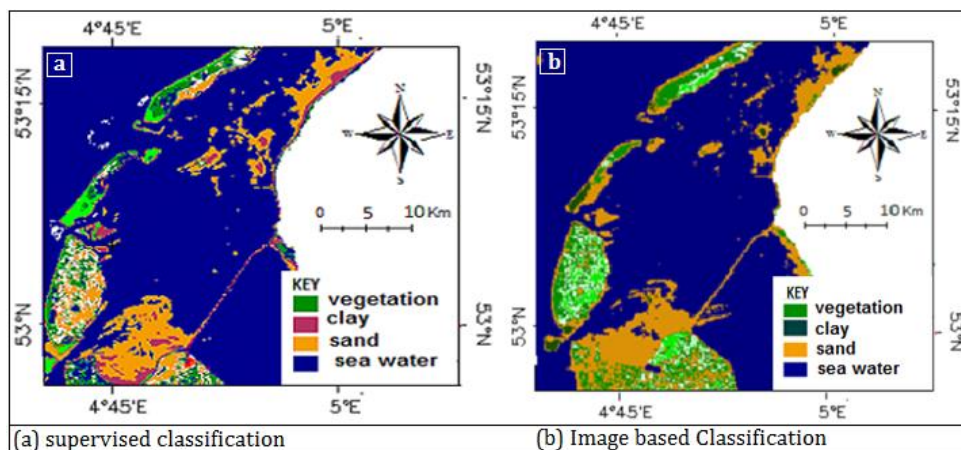


Figure 14. Intertidal mudflats sediment classes derived from use of MERIS 2011.

Table 2. Summary of statistical tables for Image based classification.

Remotely sensed data	Sediment class	Minimum	Maximum	Mean	St. dev	ndvi
Landsat TMS 2000	Sea weeds	1.00	7.00	5.68	2.49	0.71
	Clay	0.01	2.00	1.95	0.21	0.28
	Sand	2.00	5.00	5.98	0.03	0.02
ASTER 2003	Sea weeds	0.00	8.00	7.98	0.41	0.65
	Clay	0.00	2.00	1.68	0.67	0.23
	Sand	1.00	7.00	7.00	0.08	0.02
Landsat TMS 2009	Sea weeds	0.00	5.00	4.34	1.79	0.50
	Clay	0.00	3.00	2.16	0.37	0.25
	Sand	2.00	6.00	5.87	0.61	0.01
Landsat TMS 2010	Sea weeds	0.00	4.00	0.92	1.75	0.40
	Clay	0.01	7.00	2.47	1.51	0.21
	Sand	0.00	9.00	8.74	1.53	0.02
MERIS 2011	Sea weeds	0.10	12.00	9.30	2.41	0.37
	Clay	0.60	7.97	2.47	0.35	0.13
	Sand	1.00	10.00	7.49	2.53	0.03

imagery and the lowest (0.01) was recorded in 2009 from Landsat imagery. This shows that, in year 2000 the concentration of microphytobenthic organisms, seaweeds were very high as compared to the following years (Table 2).

Conclusions

Based on our findings we come up with three conclusions:

- i) Radiometric field measurements indicate that, different sediment properties (sea weeds, clay and sand) have different spectral characteristics;
- ii) Intertidal sediment properties can be successfully derived from coarse-to-medium resolution imagery, based on the sediment inherent optical properties;
- iii) NDVI can be successfully used to validate the sediment properties classification results, with high NDVI values observed over sea weeds, clay and sand respectively.

ACKNOWLEDGEMENTS

The authors would also like to thank NASA through GloVis link, European Space Agency (ESA) and the ITC RSG lab for providing us with Landsat images, full resolution MERIS image for September 2011 and ASTER images respectively, of the study area. The anonymous

reviewers for this work are also greatly acknowledged. Thanks to Eelke Folmer (NIOZ) scientific comments during field work and after. Also, many thanks go to the Dutch Government (NUFFIC), for funding this research and ITC Faculty of Geo-Information and Earth Observation (WREM Department) for providing a conducive research environment. Moreso, the authors would like to thank the Anonymous reviewers.

REFERENCES

- Adam S, De Backer A, De Wever A, Sabbe K, Toorman EA, Vincx M, Monbaliu J (2009). Bio-physical characterization of sediment stability in mudflats using remote sensing: A laboratory experiment. *Contin. Shelf Res.* 31:S26-S35.
- Berk A, Acharya JH, Chetwynd LS, Bernstein EP, Shettle MW, Adler-Golden SM, Hanscom AFB (2000). MODTRAN 4 User's Manual. MA: Air Force Res. Lab.
- Blanchard GF (2000). The effect of geomorphological structures on potential biostabilisation by microphytobenthos on intertidal mudflats. *Contin. Shelf Res.* 20:1243-1256.
- Boardman JW (1994). Geometric mixture analysis of imaging spectrometry data. Paper presented at the Proceedings of the International Geoscience and Remote Sensing Symposium.
- Boardman JW, Kruse FA (1994). Automated spectral analysis: a geological example using AVIRIS data, North Grapevine Mountains, Nevada. Paper presented at the Proceedings of the Tenth Thematic Conference on Geological Remote Sensing.
- Brotas V, Cabrita T, Portugal A, Serôdio J, Catarino F (1995). Spatio-temporal distribution of the microphytobenthic biomass in intertidal flats of Tagus Estuary, Portugal. *Hydrobiologia* 300-301(1):93-104.
- Carrère V, Spilmont N, Davoult D (2004). Comparison of simple techniques for estimating chlorophyll a concentration in the intertidal zone using high spectral-resolution field-spectrometer data. *Mar. Ecol. Progr. Ser.* 274:31-40.

- Chander G, Markham BL, Helder DL (2009). Summary of current radiometric calibration coefficients for Landsat MSS, TM, ETM+, and EO-1 ALI sensors. *Rem. Sens. Environ.* 113:893-903.
- Chaudhry F, Chao-Cheng W, Liu W, Chang C, Plaza A (2006). Pixel purity index-based algorithms for endmember extraction from hyperspectral imagery. *Recent Advances in Hyperspectral Signal and Image Processing*.
- CPSL (2005). Coastal Protection and Sea Level Rise: Solutions for Sustainable Coastal Protection in the Wadden Sea Region. Wilhelmshaven, Germany.
- De Carvalho C, Meneses PR (2000). Spectral Correlation Mapper (SCM): An Improvement on the Spectral Angle Mapper (SAM). Summaries of the 9th JPL Airborne Earth Science Workshop: JPL Publication, 00-18:9.
- Deronde B, Kempeneer P, Forster RM (2006). Imaging spectroscopy as a tool to study sediment characteristics on a tidal sandbank in the Westerschelde. *Estuarine, Coastal, Shelf Sci.* 69:580-590.
- Dube T (2012). Primary Productivity of Intertidal mudflats in the Wadden Sea: A Remote Sensing Method. MSc University Twente-ITC, Enschede, p. 27.
- ESA (2012). BEAM Earth observation toolbox and development platform. Retrieved 11 January, 2012, from <http://www.brockmann-consult.de/cms/web/beam/>
- Felde GW, Anderson GP, Adler-Golden SM, Matthew MW, Berk A (2003). Analysis of Hyperion Data with the FLAASH Atmospheric Correction Algorithm. Algorithms and Technologies for Multispectral, Hyperspectral, and Ultraspectral Imagery IX. Paper presented at the SPIE Aerosense.
- Hogan CM (2011). Wadden Sea. *Encyclopedia of Earth*. National Council for Science and the Environment. Washington DC.
- Hommersoms A (2010). "Dense Water" and "Fluid Sand" Optical properties and methods for remote sensing of the extremely turbid Wadden Sea. Vrije Universiteit, Amsterdam.
- Jesus B, Mendes CR, Brotas V, Paterson DM (2006). Effect of sediment type on microphytobenthos vertical distribution: Modelling the productive biomass and improving ground truth measurements. *J. Exp. Mar. Biol. Ecol.* 332(1):60-74.
- Kaufmann YJ, Wald AE, Remer LA., Gao BC, Li RR Flynn L (1997). The MODIS 2.1-mm Channel-Correlation with Visible Reflectance for Use in Remote Sensing of Aerosol. *IEEE Trans. Geosci. Rem. Sens.* 35:1286-1298.
- Kromkamp J, Morris EP, Forster RM, Honeywill C, Hagerthey S, Paterson DM (2006). Relationship of Intertidal Surface Sediment Chlorophyll Concentration to Hyperspectral Reflectance and Chlorophyll Fluorescence. *Estuaries Coasts* 29(2):183-196.
- Kruse FA, Lefkoff AB, Boardman JW, Heidebrecht KB, Shapiro AT, Barloon P J, Goetz AFH (1992). The spectral image processing system (SIPS)-interactive visualization and analysis of imaging spectrometer data. *Rem. Sens. Environ.* 44(2-3):145-163.
- Kruse FA, Lefkoff AB, Boardman JW, Heidebrecht KB, Shapiro AT, Barloon PJ, Goetz AFH (1993). The Spectral Image Processing Systems (SIPS) - Interactive Visualisation and Analysis of imaging spectrometer data.
- Otto S, Zuidbroek K (2001). The Wadden Sea Region: A Unique Cultural Landscape.
- Paterson DM, Hagerthey SE (2001). Microphytobenthos in Constrasting Coastal Ecosystems: Biology and Dynamics In Reise K (Ed.). *Ecol. Comparisons Sediment. Shores* 151:105-125.
- Rahman H, Dedieu G (1994). SMAC: A simplified method for the atmospheric correction of satellite measurements in the solar spectrum. *Int. J. Rem. Sens.* 15(1):123-143.
- Reise K, Baptist M, Burbridge P, Dankers N, Fischer L, Flemming B, Smit C (2010). The Wadden Sea – A Universally Outstanding Tidal Wetland. *Wadden Sea Ecosystem*. Wilhelmshaven, Germany.
- Rulinda CM, Wietske B, Stein A (2010). Image mining for drought monitoring in eastern Africa using Meteosat SEVIRI data. *Int. J. Appl. Earth Observ. Geoinform.* 1(0):S63-S68.
- Schwengerdt RA (1997). Remote Sensing: Models and Methods for Image Processing, p. 447.
- Smith GM, Thomson AG, Moller I, Kromkamp JC (2004). Using hyperspectral imaging for the assessment of mudflat surface stability. *J Coast. Res.* 20(4):1165-1175.
- Stal LJ (2010). Microphytobenthos as a biogeomorphological force in intertidal sediment stabilization. *Ecol. Eng.* 36(2):236-245.
- Tucker C (1979). Red and photographic infrared linear combinations for monitoring vegetations. *Rem. Sens. Environ.* 8:127-150.
- Trishchenko AP, Hwang B, Li Z (2002). Atmospheric Correction of Satellite Signal in Solar Domain: Impact of Improved Molecular Spectroscopy. Paper presented at the Twelfth ARM Science Team Meeting Proceedings, St. Petersburg, Florida.
- UNEP (2009). The Wadden Sea Germany and The Netherlands. Retrieved 24 August, 2011, from http://www.unep-wcmc-apps.org/sites/wh/pdf/Wadden_Sea.pdf
- van der Wal D, Herman PMJ, Ysebaert T (2004). Space-borne synthetic aperture radar of intertidal flat surfaces as a basis for predicting benthic macrofauna distribution. *EARSeL eProceedings* 3, 69-80.
- van der Wal D, Dool W (2010). Spatial Synchrony in Intertidal Benthic Algal Biomass in Temperate Coastal and Estuarine Ecosystems. *Ecosystems* 13(2):338-351.
- YCEO (2011). ASTER images: The Yale Center for Earth Observation. Retrieved 10 November, 2011, from <http://www.yale.edu/ceo/>
- Yuhas RH, Goetz A, Boardman JW (1992). Discrimination Among Semi-Arid Landscape Endmembers Using Spectral Angle Mapper (SAM) Algorithm, Summaries of the 4th Annual JPL Airborne Geoscience Workshop. Paper presented at the AVIRIS Workshop.